

# JGR Solid Earth

## RESEARCH ARTICLE

10.1029/2020JB021511

## Pore Habit of Gas in Gassy Sediments

Marco Terzariol<sup>1</sup> , Nabil Sultan<sup>1</sup> , Ronan Apprioual<sup>1</sup>, and Sebastien Garziglia<sup>1</sup> 

<sup>1</sup>REM-GM, IFREMER, Plouzane, France

### Key Points:

- Fines content determines the global behavior of gassy and non-gassy sediments
- The pore habit in gassy sediments depends on its capability to invade a neighboring pore (capillarity) and burial depth (effective stress)
- The analysis proposed helps understand subsurface gas activity in natural marine environments, potential passageways and stagnant bubbles

### Correspondence to:

M. Terzariol,  
[marco.terzariol@ifremer.fr](mailto:marco.terzariol@ifremer.fr)

### Citation:

Terzariol, M., Sultan, N., Apprioual, R., & Garziglia, S. (2021). Pore habit of gas in gassy sediments. *Journal of Geophysical Research: Solid Earth*, 126, e2020JB021511. <https://doi.org/10.1029/2020JB021511>

Received 9 DEC 2020  
Accepted 23 APR 2021

**Abstract** Gas bubbles are widespread in seafloors and lakebeds and typically found in shallow and fine-grained sediments. Sediment properties control gas nucleation and gas migration. Gas migration and pathways have been studied mostly in clean coarse particles or fine-grained matrices. Nevertheless, both cases show very distinct geo-behaviors. Pore habit is defined by the counteracting effects of effective stress and pore-throat-dependent capillary pressure. In this article, we explore gas nucleation by CO<sub>2</sub> gas exsolution and its consequent gas-driven fractures (open-mode discontinuities) or pore invasion in binary sediments as a function of fines content (FC). We conducted physical test analogies for different FC subjected to gas exsolution. Our results highlight that the pore habit of gas in gassy sediments depends on its capability to invade a neighboring pore (capillarity) and burial depth (effective stress). We show that the load dominant fraction in binary soils can be used to estimate the dominant pore throat size. We then proposed a robust methodology to predict the pore habit of gassy sediments from its properties as defined in recent developments in soil behavior and characterization. Finally, we applied it to a real case offshore Vancouver Island.

## 1. Introduction

Gas bubbles in sediments (gassy sediments) are widespread in seafloors and lakebeds, and typically found in shallow (<100 m below surface, with exceptions of deep bottom-simulating reflectors) and fine-grained sediments (Boudreau, 2012; Boudreau et al., 2005; Huang et al., 2004; Joyce & Jewell, 2003; Kellner et al., 2005; Valentine, 2011; Walter et al., 2006). Free gas in sediments results from the microbial decomposition of organic matter (CH<sub>2</sub>O, solid) into carbon dioxide and methane (methanogenesis), which can escape the seafloor as gas flares, accumulate as free gas and as hydrate, or be consumed in the sulphate reduction zone. It has been estimated that the accumulation rate of organic carbon in oceans is in the order of 0.1 GtC·yr<sup>-1</sup>, while methane trapped as hydrate is in the order of 455 GtC up to 1,800 GtC (Ruppel & Kessler, 2017; Wallman et al., 2012 - see also; Boswell & Collett, 2011). Methane is a potent greenhouse gas. Even low amounts of gas released to the atmosphere can irreversibly affect global climate and the biosphere (Judd, 2003; Kennett & Stott, 1991; Walter et al., 2006).

Gas flares are the telltale of gas activity in the seafloor. They have been observed in several oceans and water bodies (Dupre et al., 2015; Naudts et al., 2006; Riboulot et al., 2018; Romer et al., 2012; Scandella et al., 2011). Free-gas accumulations have been proposed as mechanisms of pockmarks, craters formation, and blow-outs (Chrisodoulou et al., 2003; Max et al., 1998; Sultan et al., 2014). Gassy sediments have a significant impact on seafloor geohazards and stability (Sultan & Garziglia, 2014). Gas exsolution in fine grained sediments creates large voids which modify their original mechanical properties, including: decrease of shear modulus and bulk modulus (Wheeler & Gardner 1989), a more contractive behavior while reducing its peak strength (Sultan & Garziglia, 2014), and a drop in pre-consolidation pressure (Sultan et al., 2012).

Sediment properties control gas nucleation and migration (Boudreau et al., 2005; Sills et al., 1991; Sun & Santamarina, 2019). Gas pore habit is defined by the counteracting effects of effective stress and pore-throat-dependent capillary pressure. Fine particles (particle size <74 μm) have inherently small pore throats and high capillary pressure. A bubble formed in such conditions will displace the surrounding sediment creating gas filled voids. Conversely, clean sand (particle size >74 μm) with large pore throats (and thus low capillary pressure) will allow the new bubble to invade the neighboring pore without significantly affecting particle arrangement.

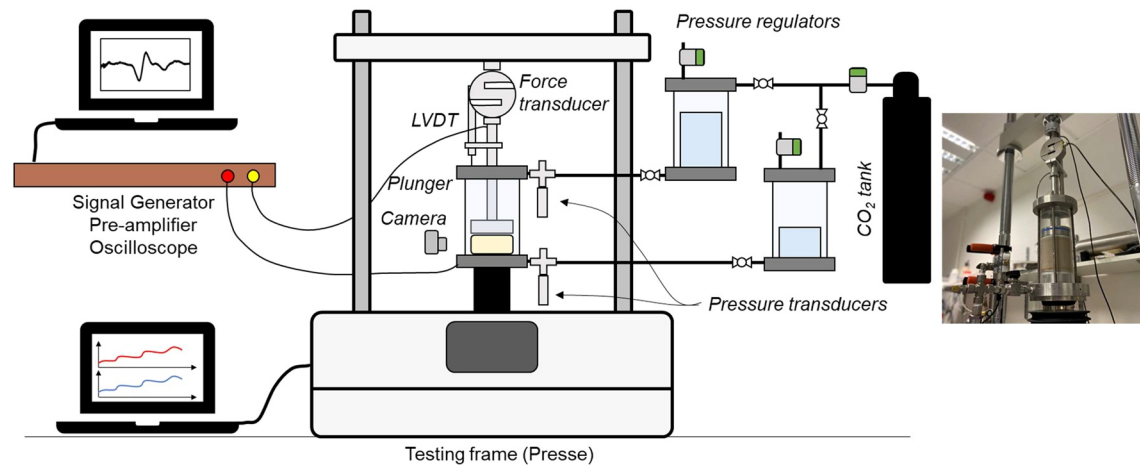


**Figure 1.** IFREMER's acrylic consolidation cell. The equipment consists of a testing frame able to apply a vertical load to the sample through a plunger. A camera captures the soil response. Bender elements in the plunger and lower pedestal can generate mechanical waves. Forces and displacements are recorded by an external force transducer and LVDT respectively, while two transducers log the pressures above and below the sample. Two peripherals complement the testing device: (a) The saturation system (right hand side) by a CO<sub>2</sub> storage tank and two intermediate containers for CO<sub>2</sub>–water saturation; (b) the mechanical wave recording system which consists of an all-in-one signal generator, a pre-amplifier and oscilloscope with direct communication to a computer.

Bubble nucleation, formation and growth in sediments is usually studied from the point of view of tensile fracture governed by linear elastic fracture mechanics, in clean coarse particles or fine-grained matrices (Clennell et al., 2000; Horseman et al., 1999; Jain & Juanes, 2009; Johnson et al., 2002, 2012, 2019; Jones, 1994; Li & Yortsos 1995; Satik et al., 1995; Sun & Santamarina, 2019; Yuan et al., 2016). Gas bubbles in sediments can be categorized as interstitial, reservoir and sediment-displacing (type I, II and III in Anderson et al., 1998) where the latter are most common. Experimental models showed contrasting modes of bubble growth: fractured media in fine-grained and pore-invasion in coarse sediments (Type III; Liu et al., 2016, 2018). Yet, in nature, soils are rarely found as clean coarse or pure fines. The transition from interstitial to sediment-displacing gas modes is not entirely understood, however it plays a central role in the hydro-mechanical behavior in a wide range of engineering problems (Jang & Santamarina, 2011). In this article, we explore gas nucleation by CO<sub>2</sub> gas exsolution in sediments and its consequent gas-driven fractures (open-mode discontinuities) or pore invasion. We develop a robust methodology to predict the pore habit of gassy sediments from its properties as defined in recent developments in soil behavior and characterization (i.e., Revised Soil Classification System [RSCS]). Finally, we extrapolate our analysis and results to explain and interpret a real case scenario offshore Vancouver Island (Cascadia Margin).

## 2. Materials and Methods

### 2.1. IFREMER Consolidation Cell

IFREMER's consolidation cell (ICC) consists of a three MPa rated transparent test cell made of a Plexiglas cylinder and two stainless steel end caps (Figure 1, see also Blouin et al., 2019). A vertical plunger can be inserted from the top cap to apply vertical load to the specimen. Two porous steel discs placed on the lower pedestal and below the plunger allow free fluid flow through the sample from two ends. Pressure transducers in both inlets capture the changes in fluid pressure. Piezocrystals and bender elements immersed in the plunger and pedestal can propagate mechanical waves ( $V_p$  and  $V_s$ ). A load cell and a linear variable differential transformer (LVDT) record the applied force and displacement, respectively. The vertical plunger builds up resistance force while loading due to pressure-dependent sealing o-rings located at the top cap and at the piston level. To account for this extra reaction, the load cell readout was calibrated from 0 up to 3 MPa water pressure and piston velocities from 0.005 mm/min up to 0.1 mm/min.

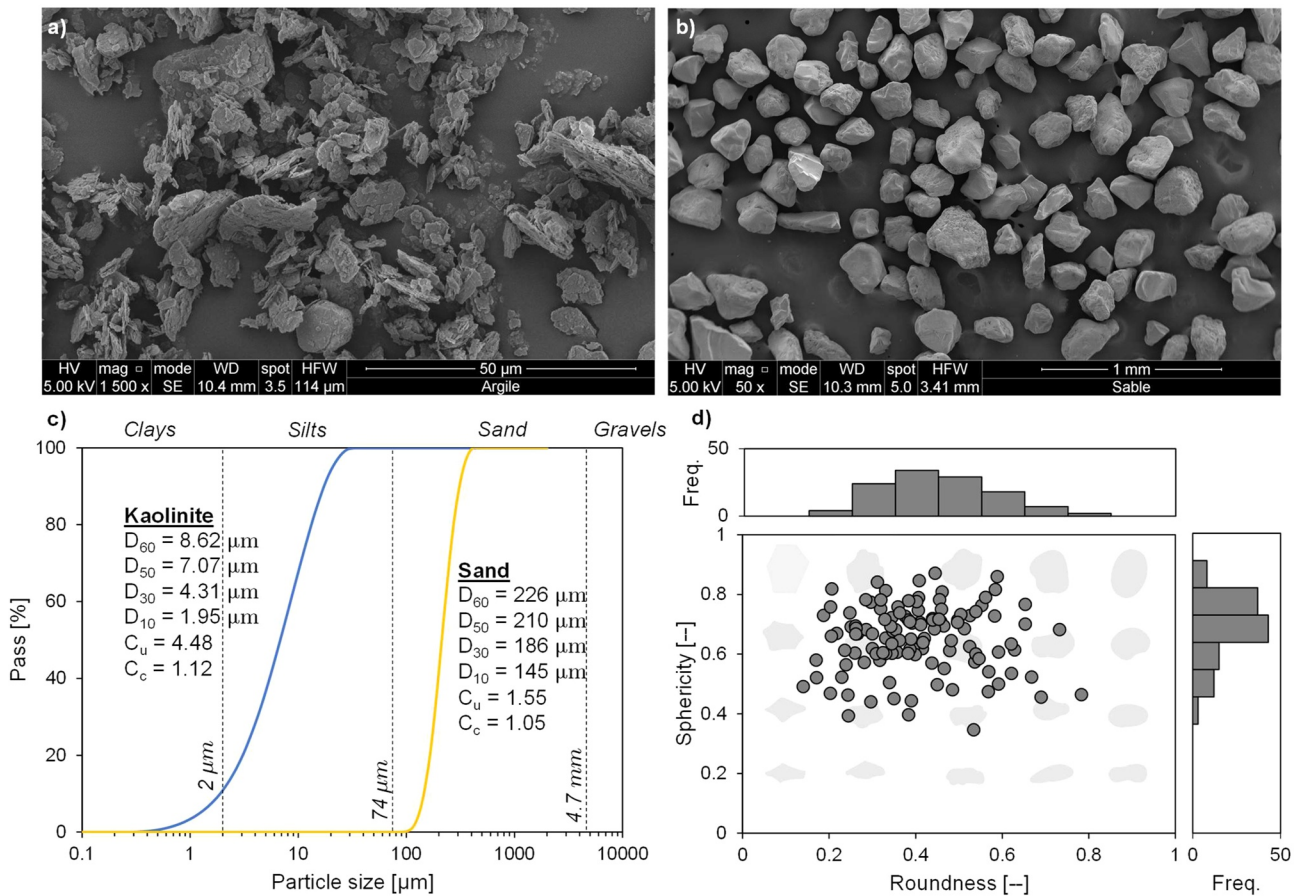


**Figure 2.** Testing soil geotechnical properties. (a) Kaolinite SEM image. (b) Sand SEM image. (c) Grain size distributions. Typical limits are superimposed (USCS). (d) Roundness R and sphericity S for sand particles by image processing of 120 particles (R and S computed as suggested by Zheng & Hryciw, 2015).

In addition, the friction between the sediment and the test cell wall (acrylic) can be significant for tall samples and low effective stresses (see Terzariol, 2015). Because the sample used in this study has a diameter of 7 cm, and the height/diameter ratio spans from 0.57 up to 1.36, the correction for sediment-wall friction can be considered negligible ( $\sigma' < 1$  kPa).

The external force is applied and controlled by a low-deformation external frame. All sensors and peripherals are connected through this frame to a dedicated computer for load control and data storage.

The testing system is completed by the carbonated water-saturation system (Figure 1). It consists of an external CO<sub>2</sub> gas cylinder connected to two half-filled transparent bottles with carbonated water. The remaining volume is completed with CO<sub>2</sub> gas. Each bottle has an individual pressure regulator for safety and pressure control.

## 2.2. Testing Soils

The unified soil classification system (USCS) utilizes the particle size 74 μm (sieve No. 200) to separate coarse and fine sediments (see also Park & Santamarina, 2017). The dominating forces acting in a particle significantly change in particle sizes in the order of 10s μm, from skeletal and self-weight forces (coarse particles) to electrically dominated capillary forces (fine particles; Santamarina et al., 2001). Thus, we use the 200-aperture sieve size as the threshold for coarse and fines particles. To prove this study's applicability, we selected two soils just above and below this boundary: Fine sand and kaolinite. The size ratios between

**Table 1**  
Testing Soils Geotechnical Properties

Property	Sym.	Kaolinite <sup>(a)</sup>	Sand <sup>(b)</sup>	Testing method
Particle size	$D_{50}$	7.07 $\mu\text{m}$	210 $\mu\text{m}$	ASTM D421 (ASTM, 2007a) and ASTM D422 (ASTM, 2007b)
	$D_{10}$	1.95 $\mu\text{m}$	145 $\mu\text{m}$	
	$C_u$	4.48	1.55	
	$C_c$	1.12	1.05	
Liquid limit	LL	59%	–	Fall cone – code: BS 1377–2 (British Standard (BS), 1990)
Plastic limit	PL	35%	–	ASTM D4318-17 (ASTM, 2017)
Roundness	R	–	0.4	SEM images and postprocessing (Zheng & Hryciw, 2015)
Sphericity	S	–	0.7	
Specific surface	$S_s$	9 $\text{m}^2/\text{gr}$	0.01 $\text{m}^2/\text{gr}$	Kaolinite: From supplier datasheet
				Sand: $S_s = 6/(D_{50} \cdot \rho_{\text{water}} \cdot G_s)$ (Santamarina et al., 2001)
Compressibility	$C_c$	0.5	–	ASTM D2435/D2435M-11 (ASTM, 2011).
	$C_s$	0.058	–	
Void ratio	$e^{\text{max}}$	$e^{10 \text{ kPa}} = 2.3$	$e_{\text{max}} = 0.75$	$e_{\text{max}}$ and $e_{\text{min}}$ estimated from $R$ and $C_u$ (Youd, 1973): $e_{\text{max}}^c = 0.032 + \frac{0.154}{R} + \frac{0.522}{C_u}$
	$e^{\text{min}}$	$e^{1 \text{ MPa}} = 0.86$	$e_{\text{min}} = 0.43$	

<sup>a</sup>Producer: SOKA (Societe Kaoliniere Armoricaire). <sup>b</sup>Producer: SIBELCO FRANCE.

particles are:  $D_{50}^{\text{coarse}}/D_{50}^{\text{fine}} \approx 30$  and  $D_{10}^{\text{coarse}}/D_{50}^{\text{fine}} \approx 20$ . Figure 2 and Table 1 summarize their individual geotechnical properties.

### 2.3. Testing Procedure

Let us consider a binary sediment mixture where the fines content (FC) is expressed as the mass of fines (MF) divided by the total sediment mass (TM) ( $\text{FC} = \text{MF}/\text{TM}$ ). To study the impact on the soil skeleton due to gas exsolution, nucleation, invasion, and open-mode discontinuities in binary mix soft sediments, we selected a broad range of FC: 0%, 1%, 2%, 10%, 15%, 20%, 25%, 30%, 35%, 50%, 60%, and 80%. Each sample was subjected to effective stresses: 0 (or self-weight), 100, 200, and 500 kPa. The testing procedure is summarized hereafter:

1. Preparation stage. The coarse-fine mixture is dry-blended. To avoid differential sedimentation, the mix is poured into ICC by 5 mm layers at the time. At each layer, the sample is mixed with carbonated water at atmospheric pressure. Once the sample is fully poured, the ICC is completed with carbonated water. The sample pore fluid is then pressurized for at least three days under no external vertical load to ensure gas dissolution.
2. Saturation stage. The sample is permeated with carbonated water under 1 MPa pressure until a full volume of pore fluid is replaced. The sample is left to rest for at least one day.
3. Loading stage. We apply the desired vertical load and allow consolidation to take place by controlling the sample deformation.
4. Degassing stage. The process of degassing involves the decrease of pore-water pressure (from the top of the sample only), and simultaneously maintaining the vertical effective stress. A camera on the side of the ICC records the full exsolution/expansion/invasion process. In the case of no external load applied, the sample deformation (and void ratio computation) is estimated by image processing (boundary tracking).
5. Re-loading. The pore fluid is re-pressurized to 1 MPa and left to rest for at least one day to ensure dissolution. Then, steps 2, 3, and 4 are repeated for a new load.
6. Steps 1–5 are repeated for each FC.

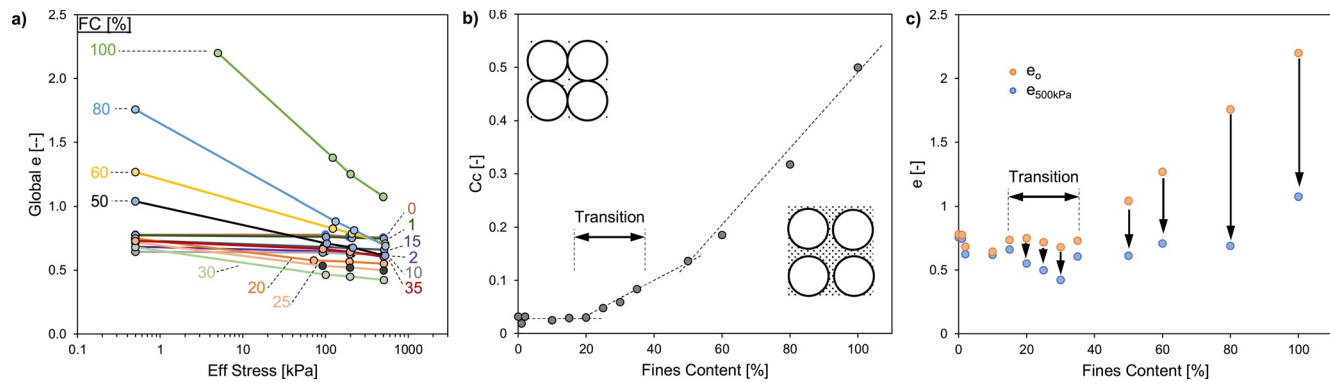


**Figure 3.** Geo-mechanical behavior of binary mixed samples (kaolinite and fine sand). (a)  $e$ - $\sigma'$  plots for each fines content (FC). (b) Compressibility index as a function of FC. The transition observed in Figure 5 is superimposed. At low FC the sample behaves as a coarse skeleton, while at high FC they displace the coarser particles, thus its compressibility increases. (c) Global void ratio  $e$  at low and high effective stress. The total deformation is evidenced by the black arrows.

It is worth noticing that in most of the tests carried out, some of the bubbles formed in previous scars left in the previous degassing stage. Nevertheless, the results shown in the next section consider only those bubbles newly formed in the skeleton matrix for the current degassing stage. In addition, to confirm our results and to avoid history-dependent scars, we re-ran the case of FC = 80% with fresh samples showing the same outcome each time.

#### 2.4. Image Binarization and Pixel Count Normalization

As exsolution takes place, the camera records video at 30 frames per second, at a resolution of  $1,280 \times 720$  pixels. Each frame is extracted and tagged with video time, elapsed test time, and fluid pressure. The following steps summarize the procedure: (a) we select and store one image every 3 kPa of fluid pressure drop; (b) crop a small section which shows a new bubble forming that best represents the general behavior of the sample; (c) subtract each image with respect to the one at  $t = 0$ ; (d) binarize the result by a unique threshold value into black and white pixels; (e) we count the amount of black pixels in each image. Black pixel count represents a semi-quantitative change in the sample due to gas exsolution with respect to the original state. Corrections due to the curved surface of the ICC in the horizontal scale were not performed in this study. In cases where there is higher quantity of gas available (i.e., large void ratio), the external light is brighter, initial sample imperfections or poor contrast, the amount of black pixels might not be comparable for different tests. To avoid these issues, we report normalized pixels count as the sum of black pixels divided by the total amount of pixels per image.

In addition, to determine global void ratio for the case where the plunger was not in contact with the sample: we tracked its expansion while the bubbles were forming via image processing. Then, we followed a similar procedure as the one described above, but this time the threshold was set to discern the boundary between the sediment and the water column. Void ratio is then computed from the evolving total volume and the sediment mass.

### 3. Results and Analyses

#### 3.1. Mixed Soils Compressibility

FC affects the sediment geo-mechanical behavior. Figure 3 summarizes each test results in terms of its compressibility index ( $C_c$ ) and void ratios. In a coarse-dominated sample, compressibility will resemble that of sand, while at higher FC, it increases with the amount of kaolinite. Between 20% and 40% of FC, the partial filling of large pores by fines increases global deformability.

#### 3.2. Nucleation Patterns

Figure 4 shows a typical degassing test for pure sand (0% fines). While at the degassing stage, we tracked changes in the sample via video imaging. Initial imperfections in the sample were used to help with particle tracking.



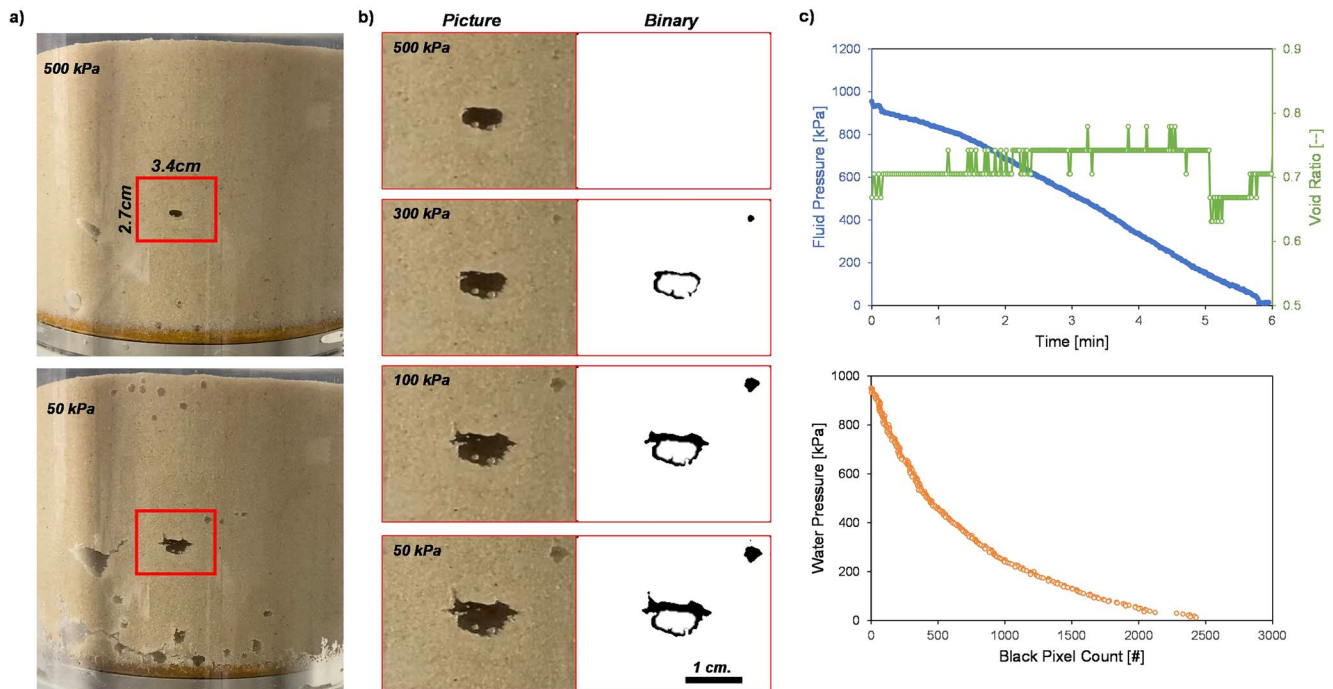


**Figure 4.** Typical degassing test (FC = 0%, and no external load applied, i.e., self-weight). (a) Full sample picture at 500 and 50 kPa of fluid pressure. (b) Image progression from 500 to 50 kPa of fluid pressure paired by its binary representation. (c) Test progression as logged. A jump in void ratio at minute 5 represents a bubble escape. From each binary image, we monitor the sample behavior by the total pixels count, and it is plotted against its current fluid pressure.

Forty-eight degassing tests were performed in this study. As expected, under no applied effective stress and for all FC, every sample reacted by opening a gas-filled void (grain-displacive): as pressure drops, gas comes out of the solution, nucleates in pores, and expands to form a cavity. The bubble expands radially until the air entry pressure is reached and invades the soil as an open-mode fracture (Figure 4b).

However, when an external load is applied, we observed different behavior and patterns at low, medium, and high FC (Figure 5):

### 3.2.1. Below 20% Fines

At a low-FC and at any applied load, the gas nucleated in pores does not open a cavity but instead invades the soil matrix in a pore-invasive mode. The gas advances faster than the case under no external load. After the degassing stage, the sample resembles an unsaturated sandy sediment (Figure 5, left panel, FC = 10%).

### 3.2.2. Above 40% Fines

At a high-FC, the behavior is fundamentally different. The gas nucleates in small pores and then expands, displacing the soil matrix (Figure 5, right panel). Smaller bubbles could also have been formed, albeit invisible to the naked eye.

### 3.2.3. Between 20% and 40% Fines

In the medium range, grain-displacive or pore-invasive mechanisms are not evident. Instead, bubbles tend to appear dispersed in locally coarser particle patches (Figure 5, middle panel). Free gas accumulations tend to be vertical rather than horizontal. The new bubble expands by invading the neighbor pore throat until it reaches a locally fine-dominated matrix which cannot invade. Then, the bubble become mobile and tends to escape upwards. This could be explained by the coalescence of neighboring bubbles. This can be seen in the pixels count for 25% fines and 100 kPa of effective stress (middle panel, Figure 5): after the gas nucleates

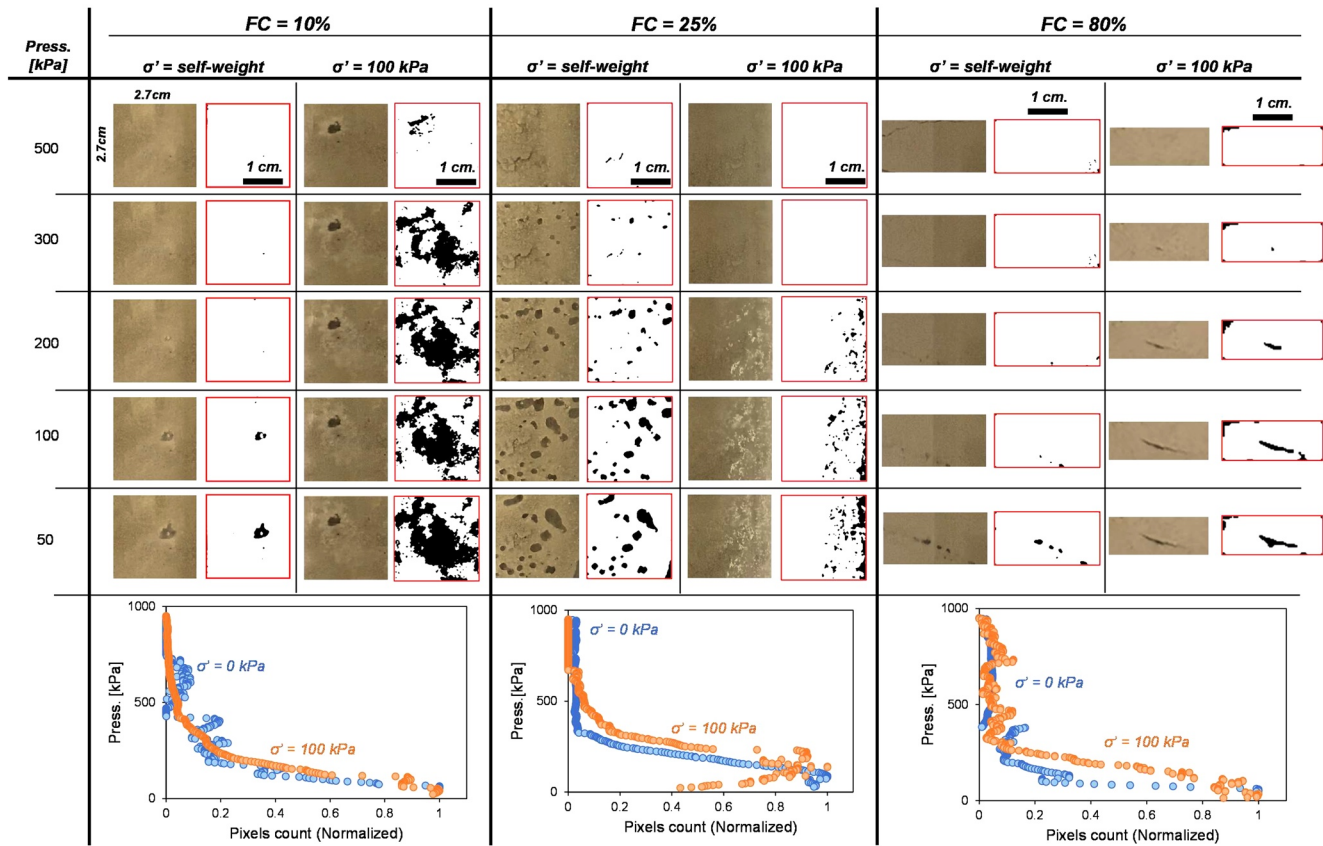


**Figure 5.** Gas exsolution, nucleation and expansion behaviors for low, intermediate, and high fines content (FC) at self-weight and 100 kPa of applied load (effective vertical stress  $\sigma'$ ). Under no applied loads, the gas expands and create a gas-filled void in a typical grain-displacive manner. When a load is applied: At low FC, the bubble expands by invading pores; at high FC by creating fractures; and at intermediate FC, by local coarse-dominated passageways.

at about 50–100 kPa of fluid pressure, a bubble escapes, decreasing rapidly the total number of pixels. This transition is superimposed in Figure 3.

A normalized pixel count summarizes the behavior of every test in Figure 6. To simplify the analysis, we divided the observations into three categories (based on visual inspection): grain-displacive, pore-invasive, and transitional. The first case can be found in all samples where no load is applied, and at high FC (blue in Figure 6), while the pore-invasive mode is dominant in low FC ( $FC \leq 20\%$ , red in Figure 6). An increase of applied load also delays the increase on pixel counts since it decreases the pore space, and consequently, the pore throat. The new bubble will require higher internal pressure to overcome the new capillary pressure counteracting its expansion.

To understand sediment expansion while degassing, we track void ratio change. In this case, we measured the global void ratio  $e$  from the total mass and the total volume occupied by the sample. At the start of each test, the pores are filled with carbonated water; thus, its concentration is the same in every test. However, since finer sediments usually have higher void ratios, there would likely be more  $CO_2$  gas available to expand while degassing. To avoid this issue, we defined a new coefficient named Degassing Expansion Coefficient (DEC) as the ratio of sample expansion due to degassing with respect to the initial global void ratio:

$$DEC = \frac{e_f - e_i}{e_i} \quad (1)$$

where  $e_f$  and  $e_i$  are the final and initial global void ratio respectively in each degassing test. Figure 7 shows the behavior of each test under effective stress. Under no external load (self-weight), the sample can expand

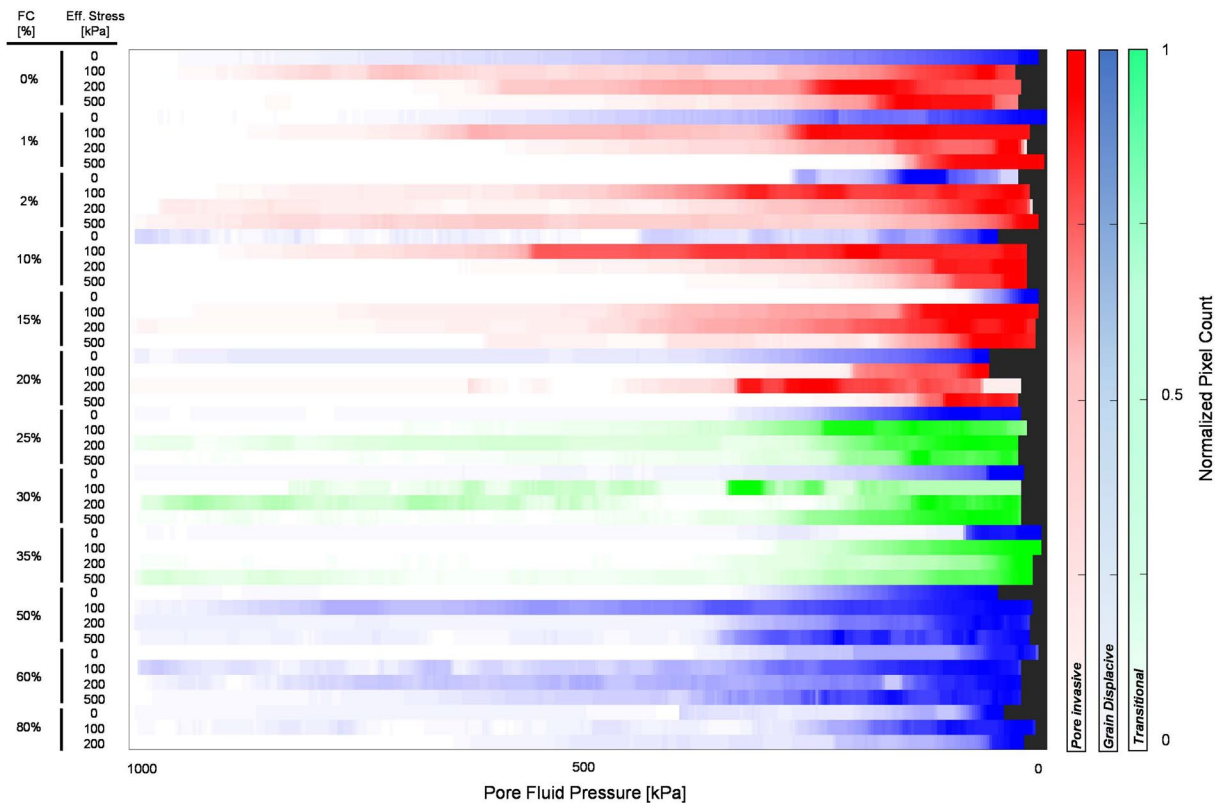


**Figure 6.** Testing summary on this study for every fines content and effective stress. Colors represent degassing habit behavior: Grain-displacive (blue), pore invasive (red), and transitional (green).

freely; the DEC is similar in all FC: grain-displacive behavior is dominant. When an external load is applied, the DEC absolute value is lower than the self-weight case, as expected. There is a slight trend of an increase in DEC with the increase of FC. This can be explained by considering that the grain-displacive mode is dominant at high FC, and a gas-filled void will render higher final global void ratios. Conversely, higher vertical loads will counteract the expansion of a bubble (open-mode), thus keeping constant the DEC. At low FC, the gas expands into pores, hindering a global change in void ratio.

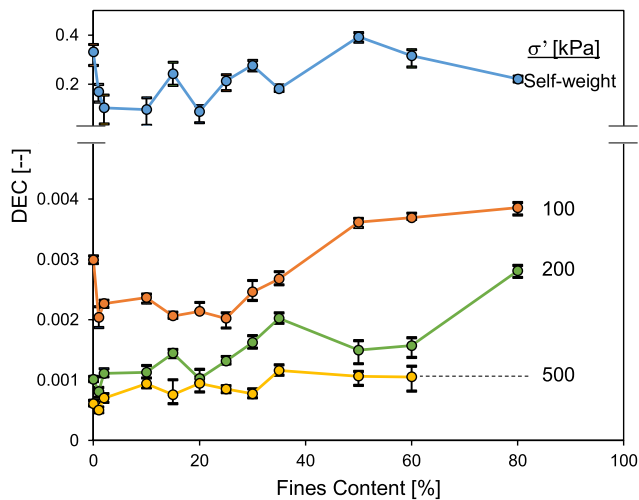


**Figure 7.** Degassing Expansion Coefficient (DEC). DEC is defined in Equation 1 as an estimation of the global soil expansion. Colors represent vertical effective stress. An increase of effective stress hinders bubble expansion. Black bars denote measurement errors.

### 3.3. Gas Exsolution Impact on the Soil Skeleton

Degassing could alter the soil structure. Shear-wave measurements can provide essential insights into pore habit. Low FC samples (FC < 20% in this study) experience both behaviors (grain-displacive and pore-invasive), thus we chose the case of clean sand to conduct shear-wave testing. Under the self-weight condition, the plunger is gently placed on top of the sample until the bender element is fully inserted without load transfer. As degassing proceeds, the bubble expands to form several grain-displacive voids. These gas-filled pockets could explain the lack of wave propagation at low fluid pressure (Figure 8). Under vertical load, the bubble forms and invades the neighbor pore and “dries” the sediment, thus water saturation decreases and interparticle forces increase. This effect is clearly reflected in the increase of shear wave velocity as the fluid pressure decreases, i.e., a stiffer skeleton (Figure 8; see also Cho & Santamarina, 2001; Whalley et al., 2012; Santamarina et al., 2001). The inflection point in shear-wave velocity appears at lower fluid pressure



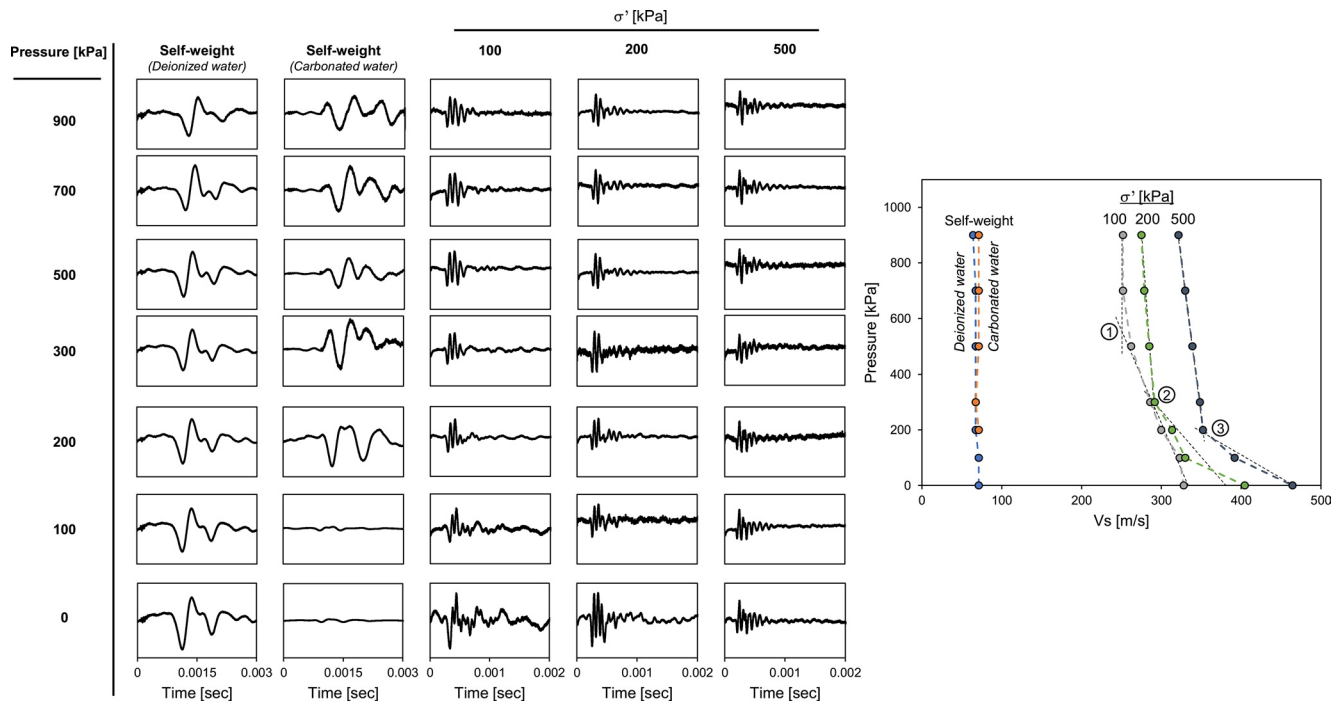


**Figure 8.** Soil skeleton behavior. Cascade of shear wave signatures for the degassing progression test of fines content (FC) = 0%. As degassing progresses, the sample with carbonated water creates large voids not allowing the wave to propagate (loss of signal). When a load is applied, shear wave velocities ( $v_s$ ) tend to increase as unsaturation takes place. However, high loads can hinder this behavior since the pore throat size depends on the effective stress, shifting the inflexion point down to 200 kPa (points 1, 2, and 3; see also Figure 6).

when the effective stress increases (points 1, 2, and 3 in right panel in Figure 8; see also Figure 6). It is worth noticing that in the case of fine-grained matrices, gas expansion is expected to damage the soil skeleton, thus decreasing shear-wave velocity.

## 4. Discussion: Gas Exsolution Driven Behavior

### 4.1. The Role of Fines

A small amount of fines can impact the dominant behavior of a mixed specimen (RSCS, Park & Santamarina, 2017; Park et al., 2018). In extreme cases (such as clean coarse or pure fines), the soil properties are clearly defined by those fractions (Figure 9). However, the amount of fines from coarse-dominated to fine-dominated behavior is not unique. The fine fraction boundaries of such transition can be defined as the void ratio of the compacted fine fraction (fine load carrier) and the void ratio of the densely packed coarse fraction (coarse load carrier). Their determination is critical for soil behavior prediction. The boundaries of the transition can be computed from each fraction void ratio ( $e_c$  = coarse fraction void ratio and  $e_f$  = fine fraction void ratio; Park & Santamarina, 2017):

$$F_F^{mech} \cong \frac{e_c}{1 + e_c + e_f} \quad (2)$$

The RSCS suggests the void ratios to use for each boundary. The first (densely packed coarse), can be found when  $e_c = e_{min}$  and  $e_f = e^{10 \text{ kPa}}$ ; while the second boundary (compacted fine fraction) is  $e_c = 1.3 \cdot e^{max}$  and  $e_f = e^{1 \text{ MPa}}$ . In this study  $e_{max}$ ,  $e_{min}$  were estimated from particle roundness  $R$  and coefficient of uniformity  $C_u$ ;  $e^{10 \text{ kPa}}$  and  $e^{1 \text{ MPa}}$  were extracted from the consolidation tests results (Table 1). Plugging these values into Equation 2, we found that for the binary testing soil the skeleton is fine-controlled when the FC is higher than 35% (Figure 9e), while it is coarse-controlled when lower than 15% (Figure 9b).

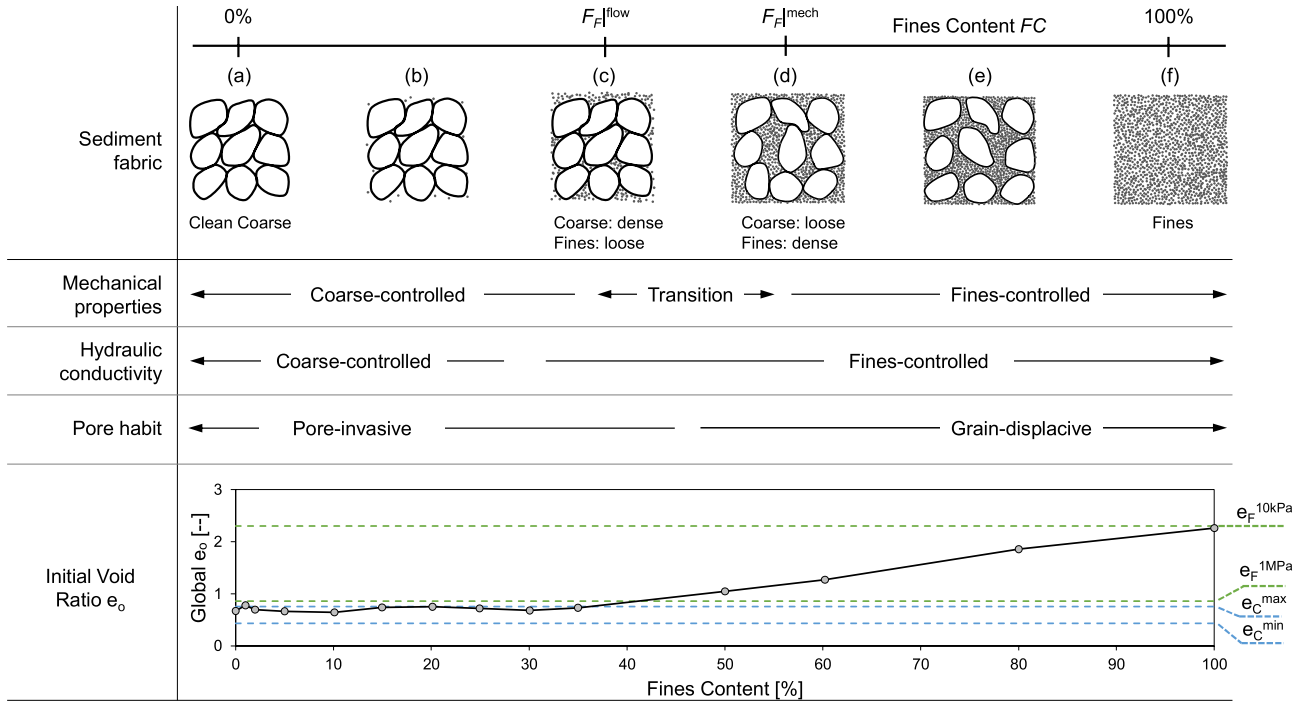


**Figure 9.** The role of fines on degassing: Mechanical properties, hydraulic conductivity, and pore habit (after Terzariol et al. 2020). Top images represent the theoretical behavior on each fines content, as conceptualized in the Revised Soil Classification System (Jang & Santamarina 2016; Park & Santamarina, 2017). Global void ratios depicted in the lower section are the measured initial void ratios in this study.

Our results show a clear transition zone in bubble growth and invasion (Figures 3–6) from FC = 20% up to 35%–40%, which compares well with the boundaries of the transition zone computed by Equation 2.

#### 4.2. Pore-Invasive Versus Grain-Displacive

Gas-filled fractures are expected when the internal pressure exceeds the minimal effective stress and skeleton tensile strength. Since these are usually unknown or difficult to obtain under in-situ conditions, we use vertical effective stress as a first-order approximation instead. Grain-displacive occurrence in sediments results from two competing forces: capillary pressure  $\Delta u$  and effective stress  $\sigma'$ . We can estimate the local behavior: higher capillary pressure with respect to the effective stress  $\Delta u > \sigma'$  will create elongated openings (grain-displacive), while the opposite condition  $\Delta u < \sigma'$  will allow gas to permeate through the soil matrix (pore invasive, see also Dai et al., 2012; Terzariol et al., 2020).

The RSCS helps defining the boundaries at which the load-carrying fraction is dominant. Then, capillary pressure can be computed from the dominating pore-throat size (or estimated from the pore size). Pore diameter  $d_p$  can be estimated from Specific Surface  $S_s$ , mineral density  $\rho_m$  and void ratio  $e$  (see Santamarina et al., 2001 and Terzariol et al., 2020 for details):

$$\text{for coarse (loose spheres)}: d_p \cong \frac{2.4}{S_s \cdot \rho_m} \quad (3)$$

$$\text{for fines (plate-like)}: d_p \cong \frac{2 \cdot e}{S_s \cdot \rho_m} \quad (4)$$

Then we can compute the capillary pressure  $\Delta u$  from the surface tension  $T_s$  ( $\text{CO}_2$  and deionized water in this study, adopted as 72 mN/m; Kim et al., 2019) and the pore diameter  $d_p$ :

$$\Delta u = \frac{4 \cdot T_s}{d_p} \quad (5)$$

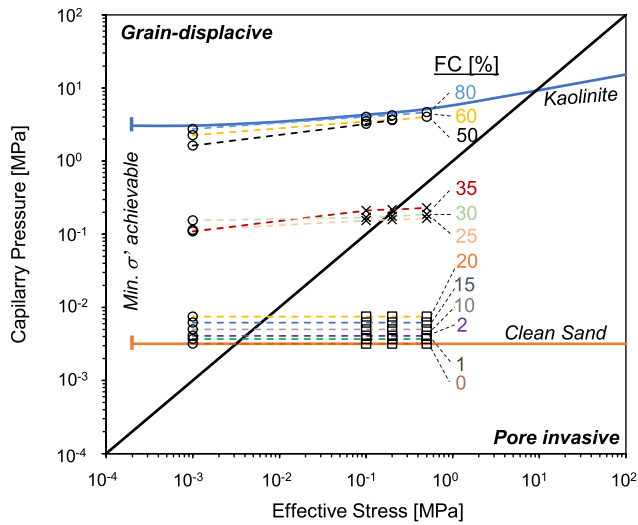


**Figure 10.** Pore invasive versus grain-displacive summary. Clean sand and pure kaolinite are computed from Equation 5. Pure kaolinite will display gas-filled voids upon degassing up until 40 MPa of effective stress. Clean sand in this study behaves as grain-displacive under self-weight condition while it is pore invasive under external loads (see also Figure 5). Circle, square and cross markers represent the observed grain-displacive, pore-invasive and transitional behavior respectively. Mixtures FC <25%, capillary pressure was computed as clean sand, however they were slightly shifted vertically for visualization purposes.

Final capillary pressure is computed by substituting Equation 3 or Equation 4 into Equation 5. In this work, clean sand renders a constant value of  $\Delta u = 3.18$  kPa. In the case of kaolinite, since void ratio varies with effective stress, capillary pressure can be computed as  $\Delta u = (7.5 \text{ MPa})/e$ . When effective stress is lower than capillary pressure, a grain-displacive mechanism can be expected: gas exsolution produces fractures up to 9 MPa of effective stress in kaolinite, while in clean sand, a pore-invasive mechanism is dominant from about 2 kPa of effective stress. We superimposed our observations to this analysis for each binary mixture (Figure 10), which shows a good agreement. The capillary pressure for each test was computed from Equations 3 and 5 for sand-dominant (FC < 25%), and Equations 4 and 5 for clay-dominant (FC > 35%) samples. For the transitional case, we weight averaged  $S_s$  with respect to FC (see also desiccation cracks below the surface, Zhao & Santamarina, 2020).

The analyses proposed in this article disregard time-dependent water diffusion into the sediment, 3D effects, volume contraction (bubble-sediment) and gas solubility upon degassing. Open-mode fracture initiation is the consequence of complex hydro-mechanical coupling that exceeds the scope of this study. However, the particle-scale approach we suggest helps understand the main driving mechanisms and estimate the essential processes in sediment degassing.

### 4.3. Implications

An expanding bubble in fine-dominated sediments could damage the soil skeleton, thus lowering its strength resistance and stiffness. However, in coarse-dominated sediments, the gas bubble invades pores without significantly modifying its structure.

The proposed approach complemented with indirect observations (seismic data, gas fronts, and gas flares), can help us estimate and identify subsurface processes. Consider a gas bubble in a sandy layer confined below a gas-tight horizon. In the deeper boundary, thanks to its large pores, the capillary pressure can be considered negligible, thus the gas shares the same pressure as the surrounding water. The bubble is not allowed to escape, thanks to the capillary pressure ( $\Delta c$ ) in the overlying layer. Thus, the internal gas pressure is given by (see Appendix for derivation):

$$u(\bar{z}) = \rho_w \cdot g \cdot z_b + \rho_{gas} \cdot g \cdot (z - z_b) \quad (6)$$

where  $\rho_w$  is water density,  $\rho_{gas}$  is the gas density and depths  $z$  are defined in Figure A1. The permeable layer skeleton is also subjected to unsaturation (supported in this study by the increase in shear wave velocity in Figure 8). The final effective stress inside the bubble must be computed from Equation 6.

### 4.4. Case Study: Cascadia Margin

To broaden and extrapolate our experimental data to natural systems, we applied our approach to the permanent and transient gas flares offshore Vancouver Island (Romer et al., 2016). Here, gas flares reach about 700 m in height, bubbling at 1,250 m below sea level. We divided the study area into four main zones (Figure 11a): (a) Zone A, where gas hydrate accumulates at shallow depths; (b) Zone B, characterized by permanent gas flares (named “Gastown Alley”) and seismic blanking at 20 m below seafloor; (c) Zone C, where the gas front in the sediment is not evident and transient gas flares are present; and (d) Zone D, a second permanent flare site (named “Bubbly Gulch”), where gas-rich sediments pinch-out into the water column.

We complemented this study with core data from the Deep-Sea Drilling Project (DSDP) Sites 889 and 890 (Westbrook et al., 1994, Figure 11b). Although these sites are located about 1.5 km from the study area,

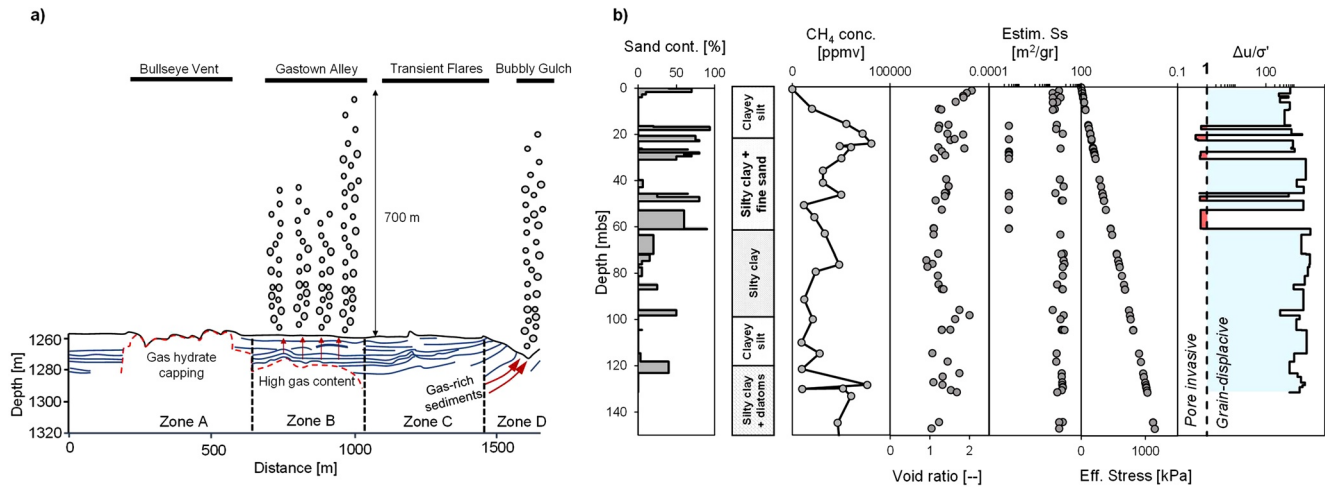


**Figure 11.** Case study: Cascadia Margin gas flares. (a) Interpreted seismic cross section of the study area (after Romer et al., 2016). (b) Selected profiles from sites 889 and 890 (Deep Sea Drilling Project; Westbrook et al., 1994): Sand content, core description, methane concentration, void ratio, estimated specific surface, computed effective stress, and interpreted  $\Delta u/\sigma'$ .

we assume similar soil descriptions and properties with the differences shown in the previous paragraph (Zones A to D). The DSDP described the top 20 m as clayey silt, followed by a ~40 m silty clay interbedded with sandy layers. The next layers correspond to silty clay (40 m thick), clayey silt (20 m thick), and silty clay with diatoms (>50 m in thickness). Unit weight ranges from 16 up to 19.5 kN/m<sup>3</sup> throughout the profile. No information was reported regarding specific surface  $S_s$ . However, we estimated  $S_s$  as a weighted average of typical values from sand content and fines mineral composition. We then computed effective stress  $\sigma'$  from depth and unit weight, and capillary pressure  $\Delta u$  from Equation 5. Results are highlighted in a blue and red profile in Figure 11b.

Our analysis shows that grain-displacive behavior is expected for most of the profile. Nevertheless, the low capillary pressure in the thin sandy layers promotes a pore-invasive mechanism. Blanking in the seismic profile and an increase in methane concentration at 20 m below seafloor in Zone B (Figure 11b) suggests a gas front at this depth. The clayey silt above might act as a seal. At this depth, we estimate a capillary pressure of 1 MPa. Assuming a gas density and water density of 90 and 997 kg/m<sup>3</sup>, respectively, we expect a bubble height in the order of 110 m (Equation 6; Figure A1). Although the existence of a massive grain-displacive bubble of such magnitude is unlikely, we can envisage a sediment matrix filled with gas-filled voids which occasionally transfer pressure from one void to another. This estimation fits well with the observed gas-driven fractures in the drilled core pictures and the constant decrease of methane concentration down to 120 m below seafloor (Figure 11b; Westbrook et al., 1994). If we assume that the bubble is located on the northern side of the study area below Zone A, then gas flares in Zone B can be explained by an open-mode fractured top clayey silt (grain-displacive mechanism). The sandy layers in the silty clay (red areas in the last profile in Figure 11b) can act as high permeability lateral pathways for gas to flow horizontally toward the “Bubbly Gulch” area (Zone D). This discharge area is in equilibrium with the water column (hydrostatic pressure), while below the seal in Zone B, the gas is over pressured at least at  $\Delta u = 1$  MPa (above the hydrostatic). Under this assumption, the gas-carrier coarse-dominated layers decrease its pressure from Zone B up to Zone D, thus hindering an escape through Zone C.

Measurements during Leg 146 also show an increase of thermogenic methane concentrations starting at 130 m below seafloor, which could be interpreted as a second bubble trapped at that depth. When this bubble finally breaks through and reaches the one on top, the newly formed bubble could increase the local gas pressure allowing gas to escape through other areas such as Zone C, hence explaining its transient condition.



## 5. Conclusions

This study explored the habit of gas bubbles in sediments as a function of FC. An image processing technique was devised to follow degassing patterns in carbonated water-saturated samples under effective stresses up to 500 kPa. Based on visual observations, we compiled our results into three categories of bubble growth: grain-displacive, pore invasive and transitional.

Our results and analyses confirm that bubble habit depends on the capability of gas to invade neighboring pores (capillarity) and burial depth (effective stress). In binary soils, the pore throat size is not unique. To estimate pore habit, we suggest first determining the load-carrying fraction (via RSCS), estimating the capillary pressure from this fraction and then comparing it with in-situ effective stress: when the effective stress is higher than the capillary pressure for the load-carrying fraction, then a pore-invasive behavior is expected. For the soils used in this study,  $F_F^{\text{mech}}$  spans 20%–35% and show a good agreement with the degassing tests. Cases where  $FC > 35\%$  open-mode discontinuities were consistently observed. This led to the identification of a transitional FC where either behavior can be expected.

The results of this study also emphasize that special attention must be considered to determine in-situ stress and behavior for sandy-gassy sediments. Bubbles are likely to be over pressured by a magnitude proportional to its height.

Finally, we utilized this approach in a real case study to understand the sediment behavior and gas flares. Our results helped understand subsurface gas activity in a natural environment, highlighting the potential passageways and conditions for stagnant bubbles to form and escape from the seafloor.

## Appendix A: Derivation of Fluid Pressure in Confined Gassy Sandy Sediments

Consider a gas stagnant bubble of height  $h$  ( $h = z_b - z_t$ ) in a sandy layer topped by gas-tight horizon (Figure 11). The pore water distribution around the bubble and the gas inside the bubble will follow the gravitational slope ( $u_w = \rho_w \cdot g \cdot z$  and  $u_{gas} = \rho_{gas} \cdot g \cdot z$ ). At the lowest point of the bubble, the pore water outside the bubble will be in direct contact with the gas. Since the layer is assumed coarse, the capillary pressure is negligible. Thus, at this point ( $z = z_b$ ) the pore water and the gas pressure can be equalized. In order to equate both equations, we will shift the gas pressure by an offset ( $O$ ) and solve (Figure 11). At  $z = z_b$ :

$$u_w |_{z_b} = u_{gas} |_{z_b}$$

$$\rho_w \cdot g \cdot z_b = \rho_{gas} \cdot g \cdot z_b + O$$

Then:

$$O = (\rho_w - \rho_{gas}) \cdot g \cdot z_b$$

The pore pressure distribution in the bubble is:

$$u(z) = \rho_w \cdot g \cdot z_b + \rho_{gas} \cdot g \cdot (z - z_b)$$

Note that when  $z = z_b \rightarrow u_{\text{bubble}} = \rho_w \cdot g \cdot z_b = u_w(z_b)$ .

The maximum difference between the bubble pressure and the pore water pressure will be at the top of the bubble, in the interface with the impermeable layer ( $z = z_t$ ):

$$u_{\text{bubble}}(z_t) = \rho_w \cdot g \cdot z_b + \rho_{gas} \cdot g \cdot (z_t - z_b)$$

$$u_w(z_t) = \rho_w \cdot g \cdot z_t$$

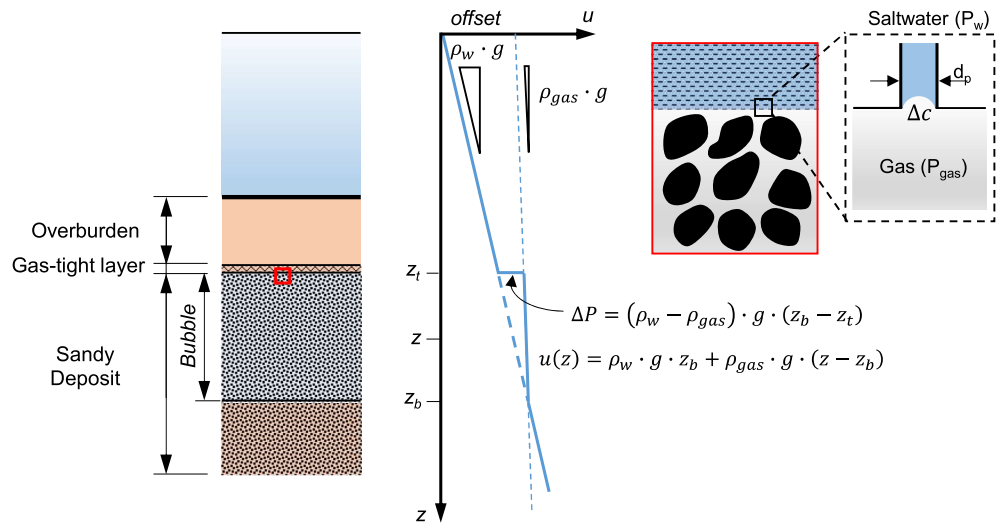


**Figure A1.** Implications on pore invasive bubble in a one-way confined sandy layer (after Espinoza & Santamarina, 2017). Pore fluid pressure in a pore-invasive trapped bubble  $u(z)$  differs considerably with respect to the hydrostatic pressure ( $\rho_w \cdot g$ ). The trapping mechanism is due to the capillary pressure of the seal ( $\Delta c$ ) which must be compared with the gas overpressure ( $\Delta P$ ).

We now can compute determine the max pressure difference as:

$$\Delta P = u_{bubble}(z_t) - u_w(z_t) = \rho_w \cdot g \cdot z_b + \rho_{gas} \cdot g \cdot (z_t - z_b) - \rho_w \cdot g \cdot z_t$$

$$\Delta P = (\rho_w - \rho_{gas}) \cdot g \cdot (z_b - z_t)$$

## Data Availability Statement

Data is available in Mendeley Data ([data.mendeley.com](https://data.mendeley.com); Terzariol 2021a, 2021b, 2021c, and 2021d).

## Acknowledgments

The authors would like to thank Shane Murphy for his insightful comments, Natalia Vazquez Riveiros and Abdeldjalyl Naoufel Haddam for the SEM images, Mickael Rovere for grain-size distribution data, and La Societe Kaoliniere Armoricaire (SOKA) for providing the kaolinite for testing. Alison Chalm edited this manuscript.

## References

- Anderson, A. L., Abegg, F., Hawkins, J. A., Duncan, M. E., & Lyons, A. P. (1998). Bubble populations and acoustic interaction with the gassy floor of Eckernförde Bay. *Continental Shelf Research*, 18(14–15), 1807–1838. [https://doi.org/10.1016/s0278-4343\(98\)00059-4](https://doi.org/10.1016/s0278-4343(98)00059-4)
- ASTM (American Society for Testing and Materials). (2007a). *Standard practice for dry preparation of soil samples for particle-size analysis and determination of soil constants. ASTM D421-85*, West Conshohocken, PA. ASTM International.
- ASTM (American Society for Testing and Materials). (2007b). *Standard test method for particle-size analysis of soils. ASTM D422-63*, West Conshohocken, PA. ASTM International.
- ASTM (American Society for Testing and Materials). (2011). *Standard test methods for one-dimensional consolidation properties of soils using incremental loading ASTM D2435/D2435M-11*, West Conshohocken, PA. ASTM International.
- ASTM (American Society for Testing and Materials). (2017). *Standard test methods for liquid limit, plastic limit, and plasticity index of soils. ASTM D4318-17*, West Conshohocken, PA. ASTM International.
- Blouin, A., Sultan, N., Callot, J.-P., & Imbert, P. (2019). Sediment damage caused by gas exsolution: A key mechanism for mud volcano formation. *Engineering Geology*, 263, 105313. <https://doi.org/10.1016/j.enggeo.2019.105313>
- Boswell, R., & Collett, T. S. (2011). Current perspectives on gas hydrate resources. *Energy & Environmental Science*, 4(4), 1206–1215. <https://doi.org/10.1039/c0ee00203h>
- Boudreau, B. P. (2012). The physics of bubbles in surficial, soft, cohesive sediments. *Marine and Petroleum Geology*, 38(1), 1–18. <https://doi.org/10.1016/j.marpetgeo.2012.07.002>
- Boudreau, B. P., Algar, C., Johnson, B. D., Croudace, I., Reed, A., Furukawa, Y., et al. (2005). Bubble growth and rise in soft sediments. *Geology*, 33(6), 517–520. <https://doi.org/10.1130/g21259.1>
- British Standard (BS) (1990). *Soils for civil engineering purposes – Part 2: Classification tests. BS 1377-2*, London. British Standard Institute.
- Cho, G. C., & Santamarina, J. C. (2001). Unsaturated particulate materials—Particle-level studies. *Journal of Geotechnical and Geoenvironmental Engineering*, 127(1), 84–96.
- Christodoulou, D., Papatheodorou, G., Ferentinos, G., & Masson, M. (2003). Active seepage in two contrasting pockmark fields in the Patras and Corinth gulfs, Greece. *Geo-Marine Letters*, 23(3–4), 194–199. <https://doi.org/10.1007/s00367-003-0151-0>
- Clennell, M. B., Judd, A., & Hovland, M. (2000). Movement and accumulation of methane in marine sediments: Relation to gas hydrate systems. In *Natural gas hydrate*, Dordrecht. Springer, (pp. 105–122).

- Dai, S., Santamarina, J. C., Waite, W. F., & Kneafsey, T. J. (2012). Hydrate morphology: Physical properties of sands with patchy hydrate saturation. *Journal of Geophysical Research*, 117(B11), B11205. <https://doi.org/10.1029/2012jb009667>
- Dupré, S., Scalabrin, C., Grall, C., Augustin, J. M., Henry, P., Şengör, A. M. C., et al. (2015). Tectonic and sedimentary controls on wide-spread gas emissions in the Sea of Marmara: Results from systematic, shipborne multibeam echo sounder water column imaging. *Journal of Geophysical Research: Solid Earth*, 120(5), 2891–2912. <https://doi.org/10.1002/2014jb011617>
- Espinoza, D. N., & Santamarina, J. C. (2017). CO<sub>2</sub> breakthrough—Caprock sealing efficiency and integrity for carbon geological storage. *International Journal of Greenhouse Gas Control*, 66, 218–229. <https://doi.org/10.1016/j.ijggc.2017.09.019>
- Horseman, S. T., Harrington, J. F., & Sellin, P. (1999). Gas migration in clay barriers. *Engineering Geology*, 54(1–2), 139–149. [https://doi.org/10.1016/s0013-7952\(99\)00069-1](https://doi.org/10.1016/s0013-7952(99)00069-1)
- Huang, Y., Zhang, W., Zheng, X., Li, J., & Yu, Y. (2004). Modeling methane emission from rice paddies with various agricultural practices. *Journal of Geophysical Research*, 109(D8), D08113.
- Jain, A. K., & Juanes, R. (2009). Preferential mode of gas invasion in sediments: Grain-scale mechanistic model of coupled multiphase fluid flow and sediment mechanics. *Journal of Geophysical Research*, 114, B08101. <https://doi.org/10.1029/2008JB006002>
- Jang, J., & Santamarina, J. C. (2011). Recoverable gas from hydrate-bearing sediments: Pore network model simulation and macro-scale analyses. *Journal of Geophysical Research*, 116(B8), B08202. <https://doi.org/10.1029/2010jb007841>
- Jang, J., & Santamarina, J. C. (2016). Fines classification based on sensitivity to pore-fluid chemistry. *Journal of Geotechnical and Geoenvironmental Engineering*, 142(4), 06015018.
- Johnson, B. D., Barry, M. A., Boudreau, B. P., Jumars, P. A., & Dorgan, K. M. (2012). In situ tensile fracture toughness of surficial cohesive marine sediments. *Geo-Marine Letters*, 32, 39–48. <https://doi.org/10.1007/s00367-011-0243-1>
- Johnson, B. D., Boudreau, B. P., Gardiner, B. S., & Maass, R. (2002). Mechanical response of sediments to bubble growth. *Marine Geology*, 187, 347–363. [https://doi.org/10.1016/s0025-3227\(02\)00383-3](https://doi.org/10.1016/s0025-3227(02)00383-3)
- Johnson, M., Peakall, J., Fairweather, M., Barnes, M., Davison, S., Jia, X., et al. (2019). Sediment microstructure and the establishment of gas migration pathways during bubble growth. *Environmental Science & Technology*, 53(21), 12882–12892. <https://doi.org/10.1021/acs.est.9b03034>
- Jones, M. (1994). Mechanical principles of sediment deformation. In Maltman, A., (Ed.), *The geological deformation of sediments*, London. Chapman & Hall, pp. 37–71. [https://doi.org/10.1007/978-94-011-0731-0\\_2](https://doi.org/10.1007/978-94-011-0731-0_2)
- Joyce, J., & Jewell, P. W. (2003). Physical controls on methane ebullition from reservoirs and lakes. *Environmental and Engineering Geoscience*, 9(2), 167–178. <https://doi.org/10.2113/9.2.167>
- Judd, A. G. (2003). The global importance and context of methane escape from the seabed. *Geo-Marine Letters*, 23(3–4), 147–154. <https://doi.org/10.1007/s00367-003-0136-z>
- Kellner, E., Waddington, J. M., & Price, J. S. (2005). Dynamics of biogenic gas bubbles in peat: Potential effects on water storage and peat deformation. *Water Resources Research*, 41(8), W08417. <https://doi.org/10.1029/2004wr003732>
- Kennett, J. P., & Stott, L. D. (1991). Abrupt deep-sea warming, paleoceanographic changes and benthic extinctions at the end of the Palaeocene. *Nature*, 353(6341), 225–229. <https://doi.org/10.1038/353225a0>
- Kim, S., Espinoza, D. N., Jung, J., Cha, M., & Santamarina, J. C. (2019). Carbon geological storage: Coupled processes, engineering and monitoring. In *Science of carbon storage in deep saline formations*, Elsevier, (pp. 383–407). <https://doi.org/10.1016/b978-0-12-812752-0.00017-4>
- Li, X., & Yortsos, Y. C. (1995). Visualization and simulation of bubble growth in pore networks. *AIChE Journal*, 41, 214–222. <https://doi.org/10.1002/aic.690410203>
- Liu, L., De Kock, T., Wilkinson, J., Cnudde, V., Xiao, S., Buchmann, C., et al. (2018). Methane bubble growth and migration in aquatic sediments observed by X-ray  $\mu$ CT. *Environmental Science & Technology*, 52(4), 2007–2015. <https://doi.org/10.1021/acs.est.7b06061>
- Liu, L., Wilkinson, J., Koca, K., Buchmann, C., & Lorke, A. (2016). The role of sediment structure in gas bubble storage and release. *Journal of Geophysical Research: Biogeosciences*, 121(7), 1992–2005. <https://doi.org/10.1002/2016jg003456>
- Max, M. D., Dillon, W. P., Nishimura, C., & Hurdle, B. G. (1998). Sea-floor methane blow-out and global firestorm at the K-T boundary. *Geo-Marine Letters*, 18(4), 285–291. <https://doi.org/10.1007/s003670050081>
- Naudts, L., Greinert, J., Artemov, Y., Staelens, P., Poort, J., Van Rensbergen, P., & De Batist, M. (2006). Geological and morphological setting of 2778 methane seeps in the Dnepr paleo-delta, northwestern Black Sea. *Marine Geology*, 227(3–4), 177–199. <https://doi.org/10.1016/j.margeo.2005.10.005>
- Park, J., Castro, G. M., & Santamarina, J. C. (2018). Closure to "Revised Soil Classification System for Coarse-Fine Mixtures" by Junghee Park and J. Carlos Santamarina. *Journal of Geotechnical and Geoenvironmental Engineering*, 144(8), 07018019. [https://doi.org/10.1061/\(asce\)gt.1943-5606.0001908](https://doi.org/10.1061/(asce)gt.1943-5606.0001908)
- Park, J., & Santamarina, J. C. (2017). Revised soil classification system for coarse-fine mixtures. *Journal of Geotechnical and Geoenvironmental Engineering*, 143(8), 04017039. [https://doi.org/10.1061/\(asce\)gt.1943-5606.0001705](https://doi.org/10.1061/(asce)gt.1943-5606.0001705)
- Riboulot, V., Ker, S., Sultan, N., Thomas, Y., Marsset, B., Scalabrin, C., et al. (2018). Freshwater lake to salt-water sea causing widespread hydrate dissociation in the Black Sea. *Nature Communications*, 9(1), 1–8. <https://doi.org/10.1038/s41467-017-02271-z>
- Römer, M., Riedel, M., Scherwath, M., Heesemann, M., & Spence, G. D. (2016). Tidally controlled gas bubble emissions: A comprehensive study using long-term monitoring data from the NEPTUNE cabled observatory offshore Vancouver Island. *Geochemistry, Geophysics, Geosystems*, 17(9), 3797–3814. <https://doi.org/10.1002/2016gc006528>
- Römer, M., Sahling, H., Pape, T., Bohrmann, G., & Spieß, V. (2012). Quantification of gas bubble emissions from submarine hydrocarbon seeps at the Makran continental margin (offshore Pakistan). *Journal of Geophysical Research*, 117(C10), C10015. <https://doi.org/10.1029/2011jc007424>
- Ruppel, C. D., & Kessler, J. D. (2017). The interaction of climate change and methane hydrates. *Reviews of Geophysics*, 55, 126–168. <https://doi.org/10.1002/2016RG000534>
- Santamarina, J. C., Klein, K. A., & Fam, M. A. (2001). *Soils and waves*. New York: J. Wiley & Sons.
- Satik, C., Li, X., & Yortsos, Y. C. (1995). Scaling of single-bubble growth in a porous medium. *Physical Review E - Statistical Physics, Plasmas, Fluids, and Related Interdisciplinary Topics*, 51, 3286–3295. <https://doi.org/10.1103/physreve.51.3286>
- Scandella, B. P., Varadharajan, C., Hemond, H. F., Ruppel, C., & Juanes, R. (2011). A conduit dilation model of methane venting from lake sediments. *Geophysical Research Letters*, 38(6), L06408. <https://doi.org/10.1029/2011gl046768>
- Sills, G. C., Wheeler, S. J., Thomas, S. D., & Gardner, T. N. (1991). Behavior of offshore soils containing gas bubbles. *Géotechnique*, 41(2), 227–241. <https://doi.org/10.1680/geot.1991.41.2.227>
- Sultan, N., Bohrmann, G., Ruffine, L., Pape, T., Riboulot, V., Colliat, J.-L., et al. (2014). Pockmark formation and evolution in deep water Nigeria: Rapid hydrate growth versus slow hydrate dissolution. *Journal of Geophysical Research: Solid Earth*, 119(4), 2679–2694. <https://doi.org/10.1002/2013jb010546>

- Sultan, N., De Gennaro, V., & Puech, A. (2012). Mechanical behavior of gas-charged marine plastic sediments. *Géotechnique*, 62(9), 751–766. <https://doi.org/10.1680/geot.12.OG.002>
- Sultan, N., & Garziglia, S. (2014). Mechanical behavior of gas-charged fine sediments: Model formulation and calibration. *Géotechnique*, 64(11), 851–864. <https://doi.org/10.1680/geot.13.P.125>
- Sun, Z., & Santamarina, J. C. (2019). Grain-displacive gas migration in fine-grained sediments. *Journal of Geophysical Research: Solid Earth*, 124(3), 2274–2285. <https://doi.org/10.1029/2018jb016394>
- Terzariol, M. (2015). *Laboratory and field characterization of hydrate bearing sediments-implications*. Doctoral dissertation, Georgia Institute of Technology.
- Terzariol, M. (2021a). *Pore Habit of Gas in Gassy Sediments - Database (Part 1)*, Mendeley Data, V1. <https://doi.org/10.17632/k6fnjdjm8g.1>
- Terzariol, M. (2021b). *Pore Habit of Gas in Gassy Sediments - Database (Part 2)*, Mendeley Data, V1. <https://doi.org/10.17632/c4j3hpx6vk.1>
- Terzariol, M. (2021c). *Pore Habit of Gas in Gassy Sediments - Database (Part 3)*, Mendeley Data, V1. <https://doi.org/10.17632/z992bjs5fr.1>
- Terzariol, M. (2021d). *Pore Habit of Gas in Gassy Sediments - Database (Part 4)*, Mendeley Data, V1. <https://doi.org/10.17632/bw5h7y9xk8.1>
- Terzariol, M., Park, J., Castro, G. M., & Santamarina, J. C. (2020). Methane hydrate-bearing sediments: Pore habit and implications. *Marine and Petroleum Geology*, 116, 104302. <https://doi.org/10.1016/j.marpetgeo.2020.104302>
- Valentine, D. L. (2011). Emerging topics in marine methane biogeochemistry. *Annual Review of Marine Science*, 3, 147–171. <https://doi.org/10.1146/annurev-marine-120709-142734>
- Wallmann, K., Pinero, E., Burwicz, E., Haeckel, M., Hensen, C., Dale, A., & Rüpke, L. (2012). The global inventory of methane hydrate in marine sediments: A theoretical approach. *Energies*, 5(7), 2449–2498. <https://doi.org/10.3390/en5072449>
- Walter, K. M., Zimov, S. A., Chanton, J. P., Verbyla, D., & Chapin, F. S. (2006). Methane bubbling from Siberian thaw lakes as a positive feedback to climate warming. *Nature*, 443(7107), 71–75. <https://doi.org/10.1038/nature05040>
- Westbrook, G. K., & Shipboard Scientific Party. (1994). Sites 889 and 890. In *Proceedings of the Deep Sea Drilling Project, Initial Reports*, 146, 127–239.
- Whalley, W. R., Jenkins, M., & Attenborough, K. (2012). The velocity of shear waves in unsaturated soil. *Soil and Tillage Research*, 125, 30–37. <https://doi.org/10.1016/j.still.2012.05.013>
- Wheeler, S. J., & Gardner, T. N. (1989). Elastic moduli of soils containing large gas bubbles. *Géotechnique*, 39(2), 333–342. <https://doi.org/10.1680/geot.1988.38.3.399>
- Youd, T. L. (1973). Factors controlling maximum and minimum densities of sands. In E. Selig, & R. Ladd, (Eds.), *Evaluation of relative density and its role in geotechnical projects involving cohesionless soils*, West Conshohocken, PA. ASTM International, 98–112.
- Yuan, C., Chareyre, B., & Darve, F. (2016). Pore-scale simulations of drainage in granular materials: Finite size effects and the representative elementary volume. *Advances in Water Resources*, 95, 109–124. <https://doi.org/10.1016/j.advwatres.2015.11.018>
- Zhao, B., & Santamarina, J. C. (2020). Desiccation crack formation beneath the surface. *Géotechnique*, 70(2), 181–186. <https://doi.org/10.1680/jgeot.18.t.019>
- Zheng, J., & Hryciw, R. D. (2015). Traditional soil particle sphericity, roundness and surface roughness by computational geometry. *Géotechnique*, 65(6), 494–506. <https://doi.org/10.1680/geot.14.p.192>